Enhancement and optical control of ultrafast THz conductivity in MoSe2MoS2 vertical heterostructure

Joon Seok, Hee Young, Sunil Kumar, Arvind Singh, Anand Nivedan, Sandeep Kumar, Marc Tondusson, Jérôme Degert, Jean Oberlé, Seok Joon Yun, et al.

Enhancement in optically induced ultrafast THz response of $MoSe_2MoS_2$ heterobilayer

SUNIL KUMAR,[1,*] ARVIND SINGH,[1] SANDEEP KUMAR,[1] ANAND NIVEDAN,[1] MARC TONDUSSON,[2] JÉRÔME DEGERT,[2] JEAN OBERLÉ,[2] SEOK JOON YUN,[3] YOUNG HEE LEE,[3] AND ERIC FREYSZ[2,*]

[1]*Femtosecond Spectroscopy and Nonlinear Photonics Laboratory, Department of Physics, Indian Institute of Technology Delhi, New Delhi 110016, India*
[2]*Univ. Bordeaux, CNRS, LOMA UMR 5798, 33405 Talence, France*
[3]*Center for Integrated Nanostructure Physics (CINAP), Institute for Basic Science (IBS), Sungkyunkwan University, Suwon 16419, Republic of Korea*
[*]*eric.freysz@u-bordeaux.fr; kumarsunil@physics.iitd.ac.in*

Abstract: THz conductivity of large area MoS_2 and $MoSe_2$ monolayers as well as their vertical heterostructure, $MoSe_2MoS_2$ is measured in the 0.3-5 THz frequency range. Compared to the monolayers, the ultrafast THz reflectivity of the $MoSe_2MoS_2$ heterobilayer is enhanced many folds when optically excited above the direct band gap energies of the constituting monolayers. The free carriers generated in the heterobilayer evolve with the characteristic times found in each of the two monolayers. Surprisingly, the same enhancement is recorded in the ultrafst THz reflectivity of the heterobilayer when excited below the MoS_2 bandgap energy. A mechanism accounting for these observations is proposed.

1. Introduction

The family of two-dimensional semiconducting transition metal dichalcogenides (2D-TMDs) such as MoS_2, WS_2, $MoSe_2$ and so on, has grown significantly [1] and it is likely to remain one of the leading topics in science for many years to come due to many facets of scientific findings and knowledge they can contribute to. Heterostructures of such 2D systems offer not only a way to study their electronic properties and interlayer interactions but also provide a rich playground to expand the physics of the constituting layers [2], eventually to open enormous possibilities of utilizing them for various technological applications [3,4]. Unlike conventional semiconductor heterostructures, van der Waals (vdW) 2D heterostructures having atomically sharp interfaces are relatively easy to make either via mechanical exfoliation from bulk crystals by scotch tape method [5] or via bottom-up approaches such as using chemical vapor deposition techniques [6–8], without considering the lattice mismatch between different 2D layers. Heterostructures formed by two TMD monolayers can exhibit type-I or type-II electronic band alignments [9,10], leading to the formation of interlayer radiative excitons where the bottom of the conduction band and the top of the valence band reside in different layers. In such a case, valley lifetimes become longer than that for intralayer excitons [11,12]. More importantly, the electronic band alignment provides spatial separation of electrons and holes after photoexcitation in the heterostructures, facilitating an important virtue for their applications in photovoltaic devices [13,14]. The interfacial electronic interactions and charge transfer/separation between constituting TMDs is one of the keys to determine the characteristics of such heterostructures and hence the performance of devices made from them.

In a few reports on vertically stacked vdW heterostructures of TMDs, possible mechanisms for the charge transfer have been inferred from time-resolved optical absorption and photoluminescence studies [15–20]. Photoluminescence time-resolved spectroscopy has been

used to study the fast interlayer energy transfer in $MoSe_2/WS_2$ heterostructures [21], while ultrafast time-resolved optical pump probe spectroscopy has been used to study possible charge transfer mechanisms, including the exciton localization [22], interlayer hot excitons formation [18], and coherent charge transfer [23]. Note that all the above studies are usually done at optical photon energies above the bandgap energies of the corresponding semiconducting layers. Terahertz (THz) spectroscopy using sub-picosecond electrical transients, which is an ideal tool to study the low energy electronic processes, especially due to its sensitivity to the electrical conductivity in relevant materials for ultrafast optoelectronics, has been rarely used [24]. In fact, ultrafast THz pulses can help in investigating the time- and frequency-resolved hot charge carrier density, mobility, and photoconductivity within the heterostructure, the layers and the interfaces, in a noncontact manner to reveal their true characteristics. The THz conductivity can be modulated by modulating the free carrier density. Optical excitation by appropriate light is the most convenient way to achieve this. Moreover, the use of an ultrafast optical pulse for generating photocarriers can also provide a handle on the THz conductivity modulation in real time where the characteristic hot carrier relaxation times are underplaying. This is the prime matter of concern in our paper here.

By using sub-200 femtosecond THz pulses, we measure electrical conductivity of MoS_2 and $MoSe_2$ monolayers, and $MoSe_2MoS_2$ vertical heterostructure. Both the MoS_2 and $MoSe_2$ monolayers are direct bandgap semiconductors which form a vdW heterostructure with type–II electronic band arrangement. The static THz conductivity of the MoS_2 monolayer is nearly zero while it is finite for the $MoSe_2$ monolayer in the entire frequency range of 0.2-5 THz. For the $MoSe_2MoS_2$ heterostructure, the THz conductivity is found to be nearly equal to the arithmetic mean of the conductivities of the two constituting layers. In sharp contrast, the dynamic THz response from THz reflectivity measurements of the optically excited $MoSe_2MoS_2$ is found to be at least an order of magnitude higher than either of the two constituting monolayers. Much importantly, by creating photocarriers only in the $MoSe_2$ layer, similar enhancement in THz response of the heterostructure is observed. It is due to the almost instantaneous movement of photoelectrons across the atomistic interface between the $MoSe_2$ and MoS_2. From the saturation of the dynamic THz response of $MoSe_2MoS_2$ at excitation photon energy of 1.55 eV, i.e., below the MoS_2-bandgap energy, we find that about 90% of the photoelectrons transiently transferred from $MoSe_2$ to MoS_2 layer.

2. Materials

Large area (~15 mm x 15 mm) monolayers of $MoSe_2$ and MoS_2 were grown on SiO_2/Si substrates by two-zone furnace atmospheric pressure chemical vapor deposition technique [25]. These were then transferred onto quartz substrates using poly(methyl methacrylate) assisted wet-etching method. The $MoSe_2MoS_2$-heterobilayer was fabricated by transferring $MoSe_2$ layer onto the MoS_2 sample. The lateral size of the almost uniform monolayers of MoS_2 and $MoSe_2$ and their heterobilayer, $MoSe_2MoS_2$ on the substrates was sufficiently large for carrying out the THz experiments discussed in this paper (see supplementary information). The quality of the samples was also assessed using various techniques including Raman spectroscopy [26] and UV-Visible absorption spectroscopy.

3. Absorption and Raman spectroscopy

The respective optical absorption spectra of the TMD layers also exhibit the characteristic A-, B- and C- excitonic features, which remain intact in the $MoSe_2MoS_2$-heterobilayer (see Fig. S1 in the supplementary information). Raman spectroscopy is a tool of choice to characterize 2D-TMDs. The Raman spectra were recorded using a Thermo-Scientific DXR Raman Microscope by exciting the samples at 532 nm laser wavelength. Characteristic Raman frequencies, corresponding to the symmetric in-plane E^1_{2g} phonon and out-of-plane A_{1g} phonon modes of both the MoS_2 and $MoSe_2$ as indicated in Fig. 1(a) for all the three samples, are in excellent agreement with the reported values in the literature [27–29]. It can be seen from Fig.

1(a) that the E^1_{2g} modes of both the monolayers (288 cm^{-1} for $MoSe_2$ and 386 cm^{-1} for MoS_2) are weakly softened by ~1 cm^{-1} in the $MoSe_2MoS_2$-heterobilayer. However, the shift in the frequency of the A_{1g} mode in the latter is opposite for the MoS_2 and $MoSe_2$ monolayers, i.e., for $MoSe_2$ (242 cm^{-1}) it softens by ~1 cm^{-1}, while for MoS_2 (404 cm^{-1}) it gets hardened by a similar number. This opposite shift in the frequency of the out of plane A_{1g} mode of the two monolayers is due to the fact that MoS_2 is mechanically supported from both the sides, i.e., by $MoSe_2$ on one side and the substrate on the other. This type of opposite shift in the Raman frequencies has also been reported in the literature for MoS_2 and WS_2MoS_2 [29,30].

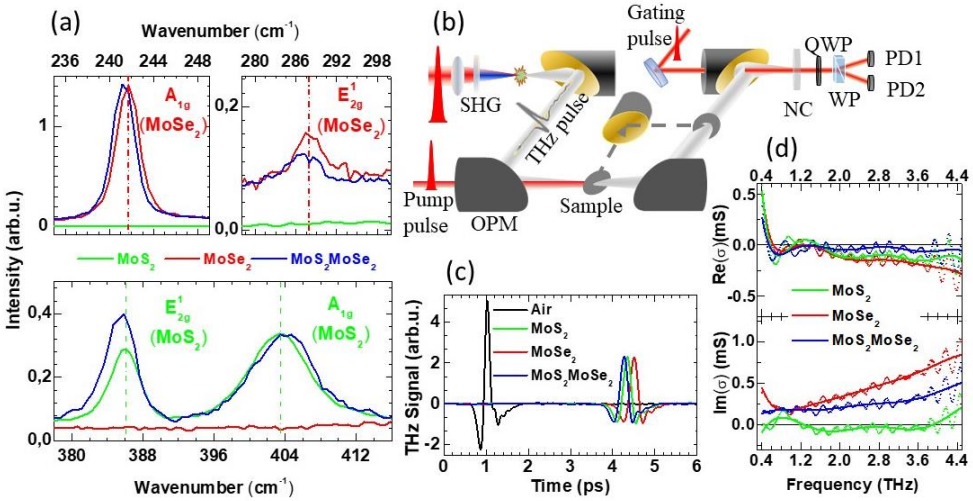

Fig. 1. Characterization and optical/THz experiments on MoS_2 monolayer, $MoSe_2$ monolayer and the $MoSe_2MoS_2$-heterobilayer, all supported on quartz substrates. **(a)** Raman spectra: vertical dashed lines to mark the positions of Raman active modes, E^1_{2g} and A_{1g}, in the monolayers and the heterobilayer. **(b)** Schematic of the experimental setup used for THz time-domain spectroscopy and optical pump-THz probe time-resolved spectroscopy in both the reflection and transmission configurations. SHG: second harmonic generation crystal, OPM: off-axis parabolic mirror, NC: nonlinear crystal for electro-optic sampling, QWP: quarter wave plate, WP: Wollaston prism, PD: photodiode. **(c)** Transmission THz time-domain traces taken in air (without any sample), MoS_2, $MoSe_2$ monolayers and the $MoSe_2MoS_2$-heterobilayer. **(d)** Real (Re(σ)) and imaginary (Im(σ)) parts of the static sheet conductivity (σ). Continuous lines represent the mean obtained using a polynomial fitting.

4. Static THz spectroscopy

Part of the experimental setup used for the measurement of static and dynamic THz response of our materials is shown in Fig. 1(b). Terahertz pulses of sub-200 fs duration were generated in air plasma and detected in a nonlinear crystal (NC) by an electro-optic sampling technique in the usual manner [31], as shown in Fig. 1(b). For driving the THz setup, femtosecond pulses with time-duration of ~50 fs were taken from a Ti:Sapphire based regenerative amplifier operating at 1 kHz repetition rate and a central wavelength (photon energy) of 800 nm (~1.55 eV). The main part of the 800 nm laser output was used to create a plasma in air by focusing the fundamental and its second harmonic from a BBO crystal, using a common biconvex lens with a 150 mm focal length. The optical beam was separated from the produced THz pulses using a highly resistive silicon wafer. A much weaker part of the femtosecond laser beam was used as sampling/gating beam for detecting/recording the THz pulses in a NC through electro-optic effect. From the source point till the detection at the nonlinear crystal, which was a 200 μm thick <110> GaP stuck on a 3 mm thick <100> GaP substrate, four silver-coated off-axis parabolic mirrors (OPMs) having focal length of 150 mm were used in a 8f imaging geometry, with the sample placed at the center between the two inner parabolic mirrors. The THz beam and gating beam are collinearly and temporally matched on the GaP crystal. Then, a combination of a quarter wave plate (QWP), a Wollaston prism (WP) and balanced photodiodes

(PDs) ensures the measurements of an electrical signal on a lock-in amplifier that is proportional to the magnitude and phase of the THz pulse falling on the GaP crystal. The complete THz setup was enclosed in a box under continuous purging of dry air to minimize THz losses from the generation point in the air-plasma till the detection point at the GaP crystal. With a few adjustments, our experimental setup allows measurements of the static and dynamic THz response.

THz time-domain scans were recorded in air, i.e., without any sample, on quartz substrate for reference and on the two monolayers and the their heterobilayer, all supported on quartz substrates. The effect of the quartz substrate was appropriately removed from the overall response of the layer samples on quartz substrates by performing reference experiments on the bare quartz plate from the same batch of substrates. Our THz experimental setup allows measurements in both the reflection and transmission modes. In each case, reference signals were also taken on the quartz substrate alone. For reflection measurements, one additional parabolic mirror and a large silver-coated plane mirror were used at f-distances as shown in the schematic of Fig. 1(b). The index of refraction $n(\Omega)$ and extinction coefficient $\kappa(\Omega)$ of the quartz substrate were determined using the standard procedure in THz time-domain spectroscopy (Fig. S3 in the supplementary information). These two parameters were used in combination with the time-domain complex electric field waveforms, $E_{THz}(t)$ as shown in Fig. 1(c) to analyze the static THz conductivity of the layers. The small temporal shift among the THz scans for the various thin samples displayed in Fig. 1(c), arises from the slight difference in the thicknesses of the quartz substrates used for each of them and checked independently. The thicknesses of the quartz substrates were 1.0444±0.0001 mm, 1.0860±0.0001 mm and 1.0153±0.0001 mm for MoS_2, $MoSe_2$ and $MoSe_2MoS_2$ samples, respectively. In fact, the mean value of the THz refractive index (n~1.9613) of the quartz substrate obtained from the temporal shifts in Fig. 1(c) and corresponding thicknesses are in perfect agreement. Though the setup in Fig. 1(b) allowed large bandwidth of ~0.2-8 THz, the losses in the quartz substrate limit the reliable evaluation of static THz conductivities of our TMD samples to ~0.2-5 THz.

The absolute values of the frequency-dependent complex sheet conductivity σ, in units of milli-Siemens (mS), of the two monolayers and their heterobilayer are presented in Fig. 1(d), where $Re(\sigma)$ and $Im(\sigma)$ are the real and imaginary parts, respectively. For extracting the complex sheet conductivity from the experimentally measured data, we used the standard thin-film approximation analysis [32]. The thick continuous curves in Fig. 1(d) are obtained using a polynomial fitting of the data and represent the mean behavior of the conductivity. It can be seen that $Re(\sigma)$ of all our samples is nearly zero within our experimental accuracy (±0.23 mS) in the entire THz frequency range. The latter uncertainty is mainly related to the uncertainty in the thickness of the quartz substrate (±0.1 μm). For the MoS_2 monolayer, $Im(\sigma)$ is almost zero while it is significantly large for the $MoSe_2$ monolayer. As expected, for the $MoSe_2MoS_2$-heterobilayer, $Im(\sigma)$ is nearly equal to the geometric mean of the values for the two constituting layers.

5. Optical pump THz probe experiment.

The THz conductivity of the layers can be modulated by modulating their free carrier density. We achieve this using sub-50 femtosecond laser pulses in the visible. The electronic bandgap energies in $MoSe_2$ and MoS_2 are ~1.3 eV and 1.9 eV, respectively. Therefore, we use optical pump pulses centered at ~3.1 eV (400 nm) and 1.55 eV (800 nm) for above and below MoS_2-bandgap photoexcitation of the $MoSe_2MoS_2$-heterobilayer. The change in transmissivity or reflectivity of the sample sensed by the THz pulse, sampled at its maximum, was recorded versus the time delay between the optical and THz pulses. From this time-resolved photoinduced reflectivity ($\Delta R(t)$) and transmittance ($\Delta T(t)$) of the THz pulses, the modulation in the THz conductivity ($\Delta\sigma(t)$) are directly inferred in real time since $\Delta\sigma \propto \Delta R$ or $-\Delta T$ [See

supplementary information]. Optical excitation at 3.1 eV generates photocarriers in both the monolayer samples and the $MoSe_2MoS_2$-heterobilayer. This modulates the photoinduced conductivity and makes it possible to infer the characteristic hot carriers' relaxation kinetics in them. Hereafter, we will only report on the experiments we performed in reflection mode. A THz echo pulse due to reflection of probe pulse from the back surface of the substrate appears at delay time of ~9ps that gets superimposed on the relaxation curves. To avoid a complex fit procedure, we restricted the analysis of the ΔR signals up to ~9 ps only, however, it is worth mentioning that all the data contain a weak and very slow relaxation components having its time constant ~100 ps (see supplementary information). The corresponding time-resolved ΔR(t) of the THz pulses at various optical pump-fluences are presented in Figs. 2(a), (d) and (g) for the $MoSe_2$ monolayer, MoS_2 monolayer and the $MoSe_2MoS_2$-heterobilayer, respectively. Thick curves in Figs. 2(a), (d) and (g) are numerical fits to the data using exponentially decaying functions convolved with a 200-fs Gaussian probe pulse (see supplementary information). Fluence dependence of the kinetic fit parameters, i.e., amplitudes (A's) and time-constants (τ's) of the relaxation components are presented in Figs. 2(b,c) for $MoSe_2$ monolayer, 2(e,f) for MoS_2 monolayer and 2(h,i) for the $MoSe_2MoS_2$. Here, the solid curves have been drawn as guide to the eyes and represent the mean behavior of the parameters. There are mainly two relaxation components, a slow one with time constant τ_1 in the range of 10-20 ps whose amplitude, A_1 gets saturated quickly at a fluence of ~60 μJ/cm^2, and another faster one (A_2,τ_2) which becomes significant at higher fluences. The amplitude, A_2 of the fast component (time-constant, τ_2 in the range of 0.8-1.2 ps) rapidly increases with the pump-fluence and gets saturated at much higher fluence value of ~150 μJ/cm^2. Besides the fact that the relaxation becomes faster at higher fluences, we note two more highlights from Fig. 2, (i) τ_1 for $MoSe_2MoS_2$ and MoS_2 are very similar, and (ii) at low fluences the magnitude of ΔR for $MoSe_2MoS_2$ is at least 3 times larger than that in any of the two layers.

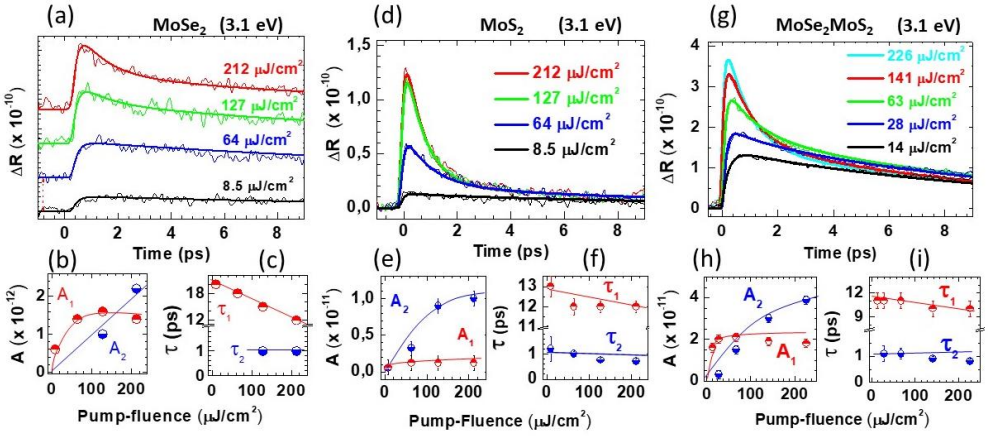

Fig. 2. Optical pump-induced transient THz reflectivity data and pump fluence dependence of the kinetic parameters recorded using optical pump at 400 nm (3.1 eV). Continuous curves in the time-resolved spectra are fits using either single exponential decay or two exponential decay components convoluted with a Gaussian pulse (200 fs FWHM). A's are amplitudes and τ's are time-constants of the exponentially decaying components. Time-resolved data at various pump fluences as mentioned in the upper panel and the corresponding exponential fit parameters as a function of the pump fluence in the lower two panels obtained for **(a-c)** $MoSe_2$, **(d-f)** MoS_2 and **(g-i)** $MoSe_2MoS_2$-heterobilayer. Consecutive time-resolved data for $MoSe_2$ in (a) are vertically shifted for better clarity. The continuous curves in the lower two panels for each sample are drawn as a guide to the eyes to represent the mean behavior of the fluence-dependence.

The characteristic time-constants, τ_1 ~ 16 ps and τ_2 ~ 1 ps in $MoSe_2$ (Figs. 2(a-c)) are similar to those reported in the literature, for example, for liquid phase exfoliated $MoSe_2$ obtained using

transient absorption spectroscopy [33]. Similarly, the two time-constant for MoS_2 in Figs. 2(d-f) also match with those from the literature [18], obtained using transient optical absorption spectroscopy. At high fluences, the appearance of the fast time constant τ_2 in all three samples (Fig. 2) is attributed to the exciton-exciton annihilation due to highly injected initial exciton density [34]. Immediately after generation of photocarriers, formation of excitons occurs naturally in these direct band gap TMD monolayers, which after a few ps, decay by emitting photoluminescence [35].

The case with optical excitation at 1.55 eV is even more interesting. In absence of photocarriers, there was absolutely no photoinduced ΔR, i.e., photoinduced THz conductivity in MoS_2 up to fluences as high as 500 $\mu J/cm^2$ (see Fig. S8 in the supplementary information). On the other hand, significant changes in $\Delta R(t)$ are obtained for $MoSe_2$ and $MoSe_2MoS_2$, as presented in Figs. 3(a) and (d) with the corresponding kinetic fit parameters shown in Figs. 3(b,c) and 3(e,f), respectively. Here also, a positive change in the photoinduced THz reflectivity, ΔR is obtained for both the $MoSe_2$ monolayer and the $MoSe_2MoS_2$-heterobilayer. Like before, the thick curves in Figs. 3(a,d) are numerical fits and dashed curves in Figs. 3(b,c) and 3(e,f) represent the mean behavior of the fluence dependence. The highlights from these results are: (i) only the slow relaxation component, (A_1,τ_1) is present up to reasonably high pump-fluences whose time constant strongly decreases with the increasing fluence, while, the saturation in its amplitude is seen at a much higher value of ~150 $\mu J/cm^2$, for both the $MoSe_2$ and $MoSe_2MoS_2$, (ii) at any given pump-fluence, the magnitude of photoinduced THz reflectivity change in $MoSe_2MoS_2$ is about four times stronger than in $MoSe_2$.

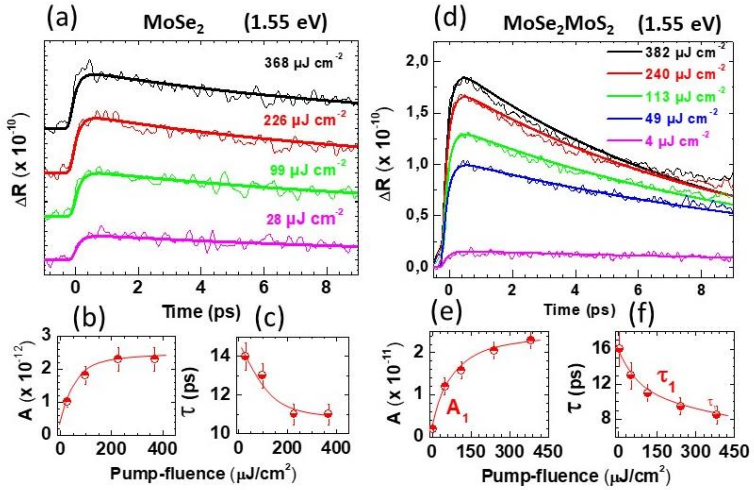

Fig. 3. Optical pump-induced transient THz reflectivity data and pump fluence dependence of the kinetic parameters recorded using optical pump at 800 nm (1.55 eV). Continuous curves in the time-resolved spectra are fits using either single or double exponential decay components convoluted with a Gaussian pulse (200 fs FWHM). A's are amplitudes and τ's are time-constants of the exponentially decaying components. Time-resolved data at various pump fluences as mentioned in the upper panel and the corresponding exponential fit parameters as a function of the pump fluence in the lower two panels obtained for **(a-c)** $MoSe_2$, **(d-f)** $MoSe_2MoS_2$-heterobilayer. The continuous curves in the lower two panels are drawn as a guide to the eyes. Consecutive time-resolved data for $MoSe_2$ in **(a)** are vertically shifted for better clarity.

6. Discussion

Consider the pictorial representations of the $MoSe_2MoS_2$-heterobilayer in real space (Fig. 4(a)) and energy space (Fig. 4(b)). Optical excitation at 3.1 eV is sufficiently high to create photoelectrons in both the layers while 1.55 eV excitation produces free carriers only in the $MoSe_2$ layer. Instantaneous displacement of the energetic photocarriers in the entire

heterostructure, including the interfacial region, should be responsible for the enhanced photoinduced THz response of $MoSe_2MoS_2$ at both the excitation photon energies used here. Assuming the out of plane velocity component of the free electrons to be ~10^5 m/s and interlayer separation of ~0.7 nm, it takes only about 10 fs for the energetic electrons to switch sides across the vdW barrier in the heterobilayer.

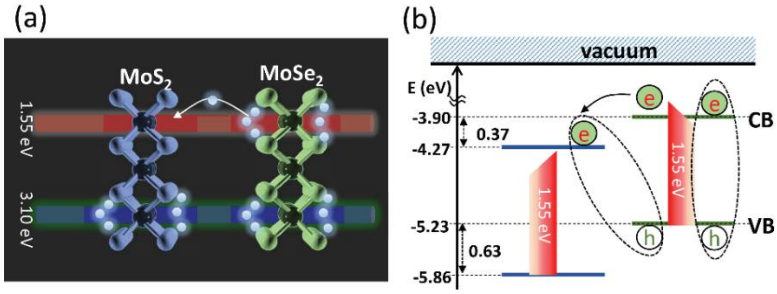

Fig. 4. (a) Schematic of the optical excitation at 1.55 eV and 3.1 eV, and **(b)** the processes related to interlayer charge transfer and formation of excitons following optical excitation at 1.55 eV which is above (below) the band gap of $MoSe_2$ (MoS_2). Along the vertical axis various energy values from vacuum have been indicated.

The electronic structures of TMD heterostructures have been computed using density functional theory by different groups and consistent numbers for the direct bandgap energy values have been reported [10,36–40]. In the $MoSe_2MoS_2$-heterobilayer, the direct bandgap energies of $MoSe_2$ and MoS_2 can be taken as ~1.3 eV and ~1.6-1.9 eV, respectively. According to DFT calculations, the number for MoS_2 is slightly smaller than what is suggested from optical absorption data [41]. Compared to MoS_2, the valence band (VB) and conduction band (CB) of $MoSe_2$ are upshifted by about ~0.63 eV and ~0.37 eV, respectively as indicated in Fig. 4(b). Consequently, like for 3.1 eV, optical excitation of the $MoSe_2MoS_2$-heterobilayer at 1.55 eV produces indirect excitons if photoelectrons are transferred from $MoSe_2$ to the MoS_2 layer as indicated in Fig. 4(b). In fact, the larger experimental time constant τ_1 in $MoSe_2MoS_2$ for 1.55 eV excitation (Fig. 3(f)) than that for 3.1 eV excitation (Fig. 2(i)) suggests a quicker and preferred route to formation of indirect excitons in the heterostructure.

The enhancement in the photoinduced THz response of the $MoSe_2MoS_2$-heterobilayer is due to the excited state ultrafast charge transfer between the two layers. This process takes place within the pump pulse duration itself, i.e., much before the intralayer relaxation through direct exciton formation, etc. begins. For the above band gap optical excitation at 3.1 eV, photocarriers are generated in both the layers. They can move across the interface between the two layers of $MoSe_2MoS_2$. The movement of the charge carriers continues proportionally up till a certain fluence, i.e., a certain photogenerated carrier density. Beyond this value of the fluence, saturation of the THz response takes place at ~60 μJ/cm^2 (Fig. 2(h)). To account for the saturation of the photoinduced THz response of the $MoSe_2MoS_2$-heterobilayer, build-up of a reverse electric field E_r has to be considered during the interlayer charge transfer at ultrafast time-scales. At high fluences, band realignment occurs between CBs of $MoSe_2$ and MoS_2 (Fig. 4(b)) which stops the further interlayer charge flow. According to this scenario, as soon as the charge transfer stops, the usual exciton formation and carrier recombination within each monolayer takes place. With the carrier recombination, the magnitude of E_r starts to reduce and CBs offset returns to its equilibrium value. In a latest work by Ma et al. [24], generation of THz pulses from above band gap optically excited $MoSe_2MoS_2$-heterobilayer was studied. The process responsible for THz generation was suggested to result from the fast interlayer charge transfer in the heterostructure taking place within 100 fs. Moreover, the amplitude of the

generated THz pulses was shown to saturate as the pump pulse fluence is increased beyond a certain value such that the CBs offset is nullified temporarily by the excessive fluence.

The above processes can be better visualized from the results obtained at optical excitation of 1.55 eV, i.e., when generation of photocarriers has taken place only in the $MoSe_2$ layer of the heterobilayer (Fig. 4) and photoelectrons' movement is unidirectional towards the MoS_2 layer. Since, within the pump-pulse duration, the carriers are moved from $MoSe_2$ to MoS_2 conduction band, the saturation fluence at this optical excitation is much larger, about 150 $\mu J.cm^{-2}$ (Fig. 3(e)). Upon saturation and nulling of the CBs offset after a while, the movement of the electrons from the $MoSe_2$ to MoS_2 stops. The electrons moved across the interface then form indirect excitons with the holes in the $MoSe_2$. A fraction of the photocarriers that still remains in the $MoSe_2$ forms direct excitons and usual intralayer relaxation process for them continues.

At 3.1 eV photoexcitation, part of the electrons can transfer from $MoSe_2$ towards MoS_2 and part of the holes from MoS_2 towards $MoSe_2$ to form indirect excitons. Saturation of the response is therefore expected to appear at a lower pump-fluence in this case. Moreover, recombination of carriers can now occur in both MoS_2 and $MoSe_2$ monolayers. Therefore, to the first approximation, a faster relaxation of the THz response at 3.1 eV optical excitation (Fig. 2(i)) as compared to that at 1.55 eV (Fig. 3(f)) is expected. At 1.55 eV optical excitation, from the absence of a fast relaxation component up to a very high excitation fluence (Fig. 3(d,e)), it is evidently clear that exciton-exciton annihilation does not take place while significant number of photoelectrons in $MoSe_2$ preferably transfer to the MoS_2 layer of the heterobilayer to form indirect excitons. The fraction of photoelectrons that transfer from $MoSe_2$ to MoS_2 can be estimated from the absorption at the pump photon energy and the corresponding saturation fluence [24]. Since the conduction band offset between $MoSe_2$ and MoS_2 is 0.37 eV (Fig. 4(b)), the reverse bias necessary to compensate for this band offset would be $V \geq 0.37$ V. This reverse bias gets developed across the interface instantly within the duration of the excitation pulse and stops the further flow of the photoelectrons. The corresponding built-in electric field would be, $E_{bi} \sim V/d \sim 0.52$ V/nm, where $d \sim 0.7$ nm is the distance between the monolayers. The photoconductivity can be given by [24] $\sigma_d \sim E_{bi}\varepsilon_0\varepsilon_T$, where ε_0 is the free space permittivity and ε_T is the out-of-plane dielectric constant. Considering $\varepsilon_T = 10$, we find the density of photoelectrons to be of $\sim 2.9\times10^{13}$ cm^{-2}. The absorption of the heterostructure at 1.55 eV is ~5% and the saturation pump fluence is ~150 $\mu J/cm^2$. From this comparison, we find that about 90% of photocarriers are transferred from $MoSe_2$ to MoS_2.

7. Conclusion

In conclusion, we firstly measured the THz conductivity of large area MoS_2 and $MoSe_2$ monolayers, and $MoSe_2MoS_2$-heterobilayer. Upon photo-excitation above the bandgap of each monolayer, we have shown that compared to the monolayers, the vertical $MoSe_2MoS_2$-heterobilayer exhibits manifold enhancement in the THz conductivity change. The relaxation time of the photo-induced carriers are very similar in the single layer and the heterostructure. Moreover, when exciting the heterostructure at 1.55 eV, about 90% of the photocarriers generated in the $MoSe_2$ are almost instantaneously transferred to MoS_2. This enhancement and optical control of the photoinduced THz response of $MoSe_2MoS_2$-heterobilayer as compared to the monolayers alone should have many implications in future electronic materials engineering for improved performance in optoelectronic applications [33]. Our results indicate that in such a TMD heterostructure an all-optical control of conductivities is possible. This opens the possibility of fast electronic components created for optimal performance at GHz to THz frequencies.

Acknowledgements

SK acknowledges SERB, Department of Science and Technology, Govt. of India for financial support through project ECR/2016/000022. IIT Delhi is acknowledged for supporting the research lab, Femtosecond Spectroscopy and Nonlinear Photonics (FemtoSpec Lab). EF acknowledges supports of the Conseil Regional Nouvelle Aquitaine and FEDER for funding the equipment of the COLA platform. YHL acknowledges the financial support by the Institute for Basic Science (IBS-R011-D1).

Disclosures

The authors declare no conflicts of interest.

References

1. S. Manzeli, D. Ovchinnikov, D. Pasquier, O. V. Yazyev, and A. Kis, "2D transition metal dichalcogenides," Nature Reviews Materials **2**, 1–15 (2017).
2. A. K. Geim and I. V. Grigorieva, "Van der Waals heterostructures," Nature **499**, 419–425 (2013).
3. M. Bernardi, M. Palummo, and J. C. Grossman, "Extraordinary Sunlight Absorption and One Nanometer Thick Photovoltaics Using Two-Dimensional Monolayer Materials," Nano Lett. **13**, 3664–3670 (2013).
4. X. Zhou, X. Hu, J. Yu, S. Liu, Z. Shu, Q. Zhang, H. Li, Y. Ma, H. Xu, and T. Zhai, "2D Layered Material-Based van der Waals Heterostructures for Optoelectronics," Adv. Funct. Mater. **28**, 1706587 (2018).
5. S. Bertolazzi, D. Krasnozhon, and A. Kis, "Nonvolatile Memory Cells Based on MoS2/Graphene Heterostructures," ACS Nano **7**, 3246–3252 (2013).
6. Y. Zhang, Y. Yao, M. G. Sendeku, L. Yin, X. Zhan, F. Wang, Z. Wang, and J. He, "Recent Progress in CVD Growth of 2D Transition Metal Dichalcogenides and Related Heterostructures," Advanced Materials **31**, 1901694 (2019).
7. Z. Cai, B. Liu, X. Zou, and H.-M. Cheng, "Chemical Vapor Deposition Growth and Applications of Two-Dimensional Materials and Their Heterostructures," Chem. Rev. **118**, 6091–6133 (2018).
8. T. Zhang and L. Fu, "Controllable Chemical Vapor Deposition Growth of Two-Dimensional Heterostructures," Chem **4**, 671–689 (2018).
9. C. Gong, H. Zhang, W. Wang, L. Colombo, R. M. Wallace, and K. Cho, "Band alignment of two-dimensional transition metal dichalcogenides: Application in tunnel field effect transistors," Appl. Phys. Lett. **103**, 053513 (2013).
10. J. Kang, S. Tongay, J. Zhou, J. Li, and J. Wu, "Band offsets and heterostructures of two-dimensional semiconductors," Appl. Phys. Lett. **102**, 012111 (2013).
11. B. Miller, A. Steinhoff, B. Pano, J. Klein, F. Jahnke, A. Holleitner, and U. Wurstbauer, "Long-Lived Direct and Indirect Interlayer Excitons in van der Waals Heterostructures," Nano Lett. **17**, 5229–5237 (2017).
12. P. Rivera, J. R. Schaibley, A. M. Jones, J. S. Ross, S. Wu, G. Aivazian, P. Klement, K. Seyler, G. Clark, N. J. Ghimire, J. Yan, D. G. Mandrus, W. Yao, and X. Xu, "Observation of long-lived interlayer excitons in monolayer MoSe2–WSe2 heterostructures," Nat Commun **6**, 6242 (2015).
13. T. Roy, M. Tosun, J. S. Kang, A. B. Sachid, S. B. Desai, M. Hettick, C. C. Hu, and A. Javey, "Field-Effect Transistors Built from All Two-Dimensional Material Components," ACS Nano **8**, 6259–6264 (2014).
14. M. M. Furchi, A. Pospischil, F. Libisch, J. Burgdörfer, and T. Mueller, "Photovoltaic Effect in an Electrically Tunable van der Waals Heterojunction," Nano Lett. **14**, 4785–4791 (2014).
15. B. Peng, G. Yu, X. Liu, B. Liu, X. Liang, L. Bi, L. Deng, T. C. Sum, and K. P. Loh, "Ultrafast charge transfer in MoS_2/WSe_2 p–n Heterojunction," 2D Mater. **3**, 025020 (2016).
16. F. Ceballos, M. Z. Bellus, H.-Y. Chiu, and H. Zhao, "Ultrafast Charge Separation and Indirect Exciton Formation in a MoS_2–$MoSe_2$ van der Waals Heterostructure," ACS Nano **8**, 12717–12724 (2014).
17. X. Hong, J. Kim, S.-F. Shi, Y. Zhang, C. Jin, Y. Sun, S. Tongay, J. Wu, Y. Zhang, and F. Wang, "Ultrafast charge transfer in atomically thin MoS2/WS2 heterostructures," Nature Nanotech **9**, 682–686 (2014).
18. H. Chen, X. Wen, J. Zhang, T. Wu, Y. Gong, X. Zhang, J. Yuan, C. Yi, J. Lou, P. M. Ajayan, W. Zhuang, G. Zhang, and J. Zheng, "Ultrafast formation of interlayer hot excitons in atomically thin MoS_2/WS_2 heterostructures," Nature Communications **7**, 1–8 (2016)
19. S. Mouri, W. Zhang, D. Kozawa, Y. Miyauchi, G. Eda, and K. Matsuda, "Thermal dissociation of inter-layer excitons in MoS_2/$MoSe_2$ hetero-bilayers," Nanoscale **9**, 6674–6679 (2017).
20. Z. Ji, H. Hong, J. Zhang, Q. Zhang, W. Huang, T. Cao, R. Qiao, C. Liu, J. Liang, C. Jin, L. Jiao, K. Shi, S. Meng, and K. Liu, "Robust Stacking-Independent Ultrafast Charge Transfer in MoS_2/WS_2 Bilayers," ACS Nano **11**, 12020–12026 (2017).
21. D. Kozawa, A. Carvalho, I. Verzhbitskiy, F. Giustiniano, Y. Miyauchi, S. Mouri, A. H. Castro Neto, K. Matsuda, and G. Eda, "Evidence for Fast Interlayer Energy Transfer in MoSe2/WS2 Heterostructures," Nano Lett. **16**, 4087–4093 (2016).
22. X. Zhu, N. R. Monahan, Z. Gong, H. Zhu, K. W. Williams, and C. A. Nelson, "Charge Transfer Excitons at van der Waals Interfaces," J. Am. Chem. Soc. **137**, 8313–8320 (2015).

23. R. Long and O. V. Prezhdo, "Quantum Coherence Facilitates Efficient Charge Separation at a MoS2/MoSe2 van der Waals Junction," Nano Lett. **16**, 1996–2003 (2016).
24. E. Y. Ma, B. Guzelturk, G. Li, L. Cao, Z.-X. Shen, A. M. Lindenberg, and T. F. Heinz, "Recording interfacial currents on the subnanometer length and femtosecond time scale by terahertz emission," Sci. Adv. **5**, eaau0073 (2019).
25. S. J. Yun, G. H. Han, H. Kim, D. L. Duong, B. G. Shin, J. Zhao, Q. A. Vu, J. Lee, S. M. Lee, and Y. H. Lee, "Telluriding monolayer MoS2 and WS2 via alkali metal scooter," Nat Commun **8**, 2163 (2017).
26. R. Saito, Y. Tatsumi, S. Huang, X. Ling, and M. S. Dresselhaus, "Raman spectroscopy of transition metal dichalcogenides," J. Phys.: Condens. Matter **28**, 353002 (2016).
27. P. Tonndorf, R. Schmidt, P. Böttger, X. Zhang, J. Börner, A. Liebig, M. Albrecht, C. Kloc, O. Gordan, D. R. T. Zahn, S. M. de Vasconcellos, and R. Bratschitsch, "Photoluminescence emission and Raman response of monolayer MoS_2, $MoSe_2$, and WSe_2," Opt. Express, OE **21**, 4908–4916 (2013).
28. J. C. Shaw, H. Zhou, Y. Chen, N. O. Weiss, Y. Liu, Y. Huang, and X. Duan, "Chemical vapor deposition growth of monolayer MoSe2 nanosheets," Nano Res. **7**, 511–517 (2014).
29. K.-G. Zhou, F. Withers, Y. Cao, S. Hu, G. Yu, and C. Casiraghi, "Raman Modes of MoS_2 Used as Fingerprint of van der Waals Interactions in 2-D Crystal-Based Heterostructures," ACS Nano **8**, 9914–9924 (2014).
30. S. Tongay, W. Fan, J. Kang, J. Park, U. Koldemir, J. Suh, D. S. Narang, K. Liu, J. Ji, J. Li, R. Sinclair, and J. Wu, "Tuning Interlayer Coupling in Large-Area Heterostructures with CVD-Grown MoS_2 and WS_2 Monolayers," Nano Lett. **14**, 3185–3190 (2014).
31. Q. Wu and X.-C. Zhang, "Free-space electro-optic sampling of terahertz beams," Applied Physics Letters **67**, 3523–3525 (1995).
32. H. J. Joyce, J. L. Boland, C. L. Davies, S. A. Baig, and M. B. Johnston, "A review of the electrical properties of semiconductor nanowires: insights gained from terahertz conductivity spectroscopy," Semicond. Sci. Technol. **31**, 103003 (2016).
33. D. B. Velusamy, R. H. Kim, S. Cha, J. Huh, R. Khazaeinezhad, S. H. Kassani, G. Song, S. M. Cho, S. H. Cho, I. Hwang, J. Lee, K. Oh, H. Choi, and C. Park, "Flexible transition metal dichalcogenide nanosheets for band-selective photodetection," Nat Commun **6**, 8063 (2015).
34. N. Kumar, Q. Cui, F. Ceballos, D. He, Y. Wang, and H. Zhao, "Exciton-exciton annihilation in MoSe 2 monolayers," Phys. Rev. B **89**, 125427 (2014).
35. H. Wang, C. Zhang, and F. Rana, "Ultrafast Dynamics of Defect-Assisted Electron–Hole Recombination in Monolayer MoS_2," Nano Lett. **15**, 339–345 (2015).
36. C. Gong, H. Zhang, W. Wang, L. Colombo, R. M. Wallace, and K. Cho, "Band alignment of two-dimensional transition metal dichalcogenides: Application in tunnel field effect transistors," Appl. Phys. Lett. **103**, 053513 (2013).
37. H. Terrones, F. López-Urías, and M. Terrones, "Novel hetero-layered materials with tunable direct band gaps by sandwiching different metal disulfides and diselenides," Sci Rep **3**, 1549 (2013).
38. L. Debbichi, O. Eriksson, and S. Lebègue, "Electronic structure of two-dimensional transition metal dichalcogenide bilayers from *ab initio* theory," Phys. Rev. B **89**, 205311 (2014).
39. C. Zhang, C. Gong, Y. Nie, K.-A. Min, C. Liang, Y. J. Oh, H. Zhang, W. Wang, S. Hong, L. Colombo, R. M. Wallace, and K. Cho, "Systematic study of electronic structure and band alignment of monolayer transition metal dichalcogenides in Van der Waals heterostructures," 2D Mater. **4**, 015026 (2016).
40. V. O. Özçelik, J. G. Azadani, C. Yang, S. J. Koester, and T. Low, "Band alignment of two-dimensional semiconductors for designing heterostructures with momentum space matching," Phys. Rev. B **94**, 035125 (2016).
41. K. F. Mak, C. Lee, J. Hone, J. Shan, and T. F. Heinz, "Atomically Thin ${\mathrm{MoS}}_{2}$: A New Direct-Gap Semiconductor," Phys. Rev. Lett. **105**, 136805 (2010).